Effect of gas composition on the oxide scale growth mechanisms in a ferritic steel for solid oxide cell interconnects

Ashok Vayyala,[1,2,3*] Ivan Povstugar,[3] Dmitry Naumenko,[4] Willem J. Quadakkers,[4] Heike Hattendorf,[5] Joachim Mayer [1,2]

[1] Ernst Ruska-Centre for Microscopy and Spectroscopy with Electrons (ER-C-2), Forschungszentrum Jülich GmbH, 52428 Jülich, Germany

[2] Central Facility for Electron Microscopy (GFE), RWTH Aachen University, Germany

[3] Central Institute for Engineering, Electronics and Analytics (ZEA-3), Forschungszentrum Jülich GmbH, 52428 Jülich, Germany

[4] Microstructure and Properties of Materials (IEK-2), Forschungszentrum Jülich GmbH, 52428 Jülich, Germany

[5] VDM Metals International GmbH, 58762 Altena, Germany

*Corresponding author: a.vayyala@fz-juelich.de

Abstract

The oxidation behavior of a ferritic steel Fe-23Cr-0.5Mn-0.6Nb-0.1Ti (at.%) considered for application in solid oxide cell (SOC) stack interconnects was studied at 800°C. The oxidation kinetics and oxide scale microstructure formed in Ar-20%O_2, Ar-4%H_2-4%H_2O and Ar-1%CO-1%CO_2 atmospheres, simulating the SOC operation environments, were investigated by thermogravimetry (TG) in conjunction with electron microscopy (SEM/TEM) and atom probe tomography (APT). In all three environments multilayered oxide scales formed, consisting of Mn-Cr spinel on top of Cr_2O_3 and an additional Nb-rich oxide layer at the chromia-alloy interface. The initially faster oxidation in the low pO_2 gases was attributed to formation of porous chromia scales compared to a dense scale formed in the high pO_2 (Ar-O_2) atmosphere. APT revealed segregation of minor alloying elements (Mn, Nb and Ti) to chromia grain boundaries in all three simulated SOC environments in quantitatively similar amounts, suggesting their similar effect on the ionic transport through the oxide scale. The findings indicate that oxygen activity in the test gas plays a dominating role in governing the oxidation kinetics and the oxide scale microstructure of the studied ferritic steel.

Keywords: SOFC, Oxide-film growth kinetics, Grain boundary segregation, Atom probe tomography (APT), STEM.

Author ORCIDs

Ashok Vayyala 0000-0002-3238-9220

Ivan Povstugar 0000-0002-1409-6854

Dmitry Naumenko 0000-0001-9026-8585

Willem J. Quadakkers 0000-0002-0644-0192

Heike Hattendorf 0000-0002-8609-0910

Joachim Mayer 0000-0003-3292-5342

1. Introduction

Solid Oxide Cell (SOC) is a general term for electrochemical devices that can operate in fuel producing as well as in power generating modes [1]. The fuel producing device is called solid oxide electrolyser cell (SOEC), which converts electric power into a chemical fuel. The power generating device is named solid oxide fuel cell (SOFC), which converts a chemical fuel (e.g. hydrogen) into electric power. In some design concepts the devices can operate in both SOEC and SOFC modes [2]. A SOC consists of an anode and a cathode separated by a solid ceramic electrolyte. During its operation in the SOFC mode, the anode-electrolyte-cathode single cell has an output voltage in the range of 0.6-0.8 V [3], which is too low for most of the considered applications. Therefore, SOC stacks are built, in which multiple cells are combined to produce the required power. For this purpose, an interconnect is an important component of a SOC stack [4], because it provides an electrical connection between the individual cells [5], as well as mechanical support and stability to the stack. The interconnect also acts as a physical barrier to separate the reactant gases, i.e. air atmosphere on the oxidant side and e.g. hydrogen or natural gas on the fuel side. The main requirements for an interconnect material are: good electrical conductivity, compatibility of thermal expansion coefficient with the ceramic electro-active components and adequate mechanical properties (yield, creep strength as well as ductility) [5]. An interconnect material must also possess very good oxidation resistance at high temperatures, i.e. form a slow growing and well adherent oxide scale, which should possess sufficient electronic conductivity to assure low contact resistance at the operating temperature. The oxide scale properties are thus vital to the overall SOC performance.

Ferritic stainless steels are typical materials considered for the interconnect application due to fulfillment of the abovementioned requirements and reasonable costs. In particular, their thermal expansion coefficients are similar to those of the commonly used anode (typically Ni-YSZ) and electrolyte (YSZ) materials [5]. In recent years a number of high-Cr (22 wt. %) ferritic stainless steels have been specifically developed for application as interconnect material for high temperature SOC applications [6,7] and are now commercially available as Crofer 22 APU and Crofer® 22 H [8–10].

The SOC interconnect steel must therefore be operating in O_2-containing, H_2-H_2O and/or CO-CO_2-containing atmospheres [1]. For instance, in an SOFC, the cathode side is exposed to O_2-rich atmosphere whereas the anode side is exposed to either H_2-H_2O or H_2-H_2O/CO-CO_2 atmospheres depending on the fuel type [11]. During high temperature oxidation at typical SOC operating temperatures between 700 to 900°C, a protective chromium-rich oxide scale grows on both surfaces of the interconnect steels [12,13]. The oxide scale composition, its growth rate and adherence to the metal depend on a number of factors, including the steel minor chemistry and the service conditions [5]. It was found that Mn alloying addition to the steel results in formation of Mn-Cr-spinel on top of the common chromia scale [9,14,15]. The spinel reduces the Cr-evaporation from the scale surface as CrO_3 or $CrO_2(OH)_2$ in atmospheres with high oxygen activities, such as prevailing at the cathode side of an SOFC or the anode side of an SOEC, and thereby enhances the overall scale stability. Ti-rich oxides were also frequently found on top of the scale indicating Ti incorporation from the base material. The presence of Ti in the chromia scale increases its electrical conductivity, an effect beneficial for the SOC-stack performance, but it also increases its growth rate [5]. Minor Nb additions, frequently added to increase the (creep) strength of ferritic stainless steels, were shown to accelerate the oxidation rate [7].

For chromia scales grown on pure chromium, binary Fe-Cr alloys as well as Ni-Cr alloys, it was found that the growth rate in high-pO_2 gases such as air or Ar-O_2 is lower than that in low-pO_2 (Ar/)H_2/H_2O [14,16]. In the former atmosphere, the dominating transport process is apparently outward metal cation diffusion. This scale growth process results in vacancy condensation at the oxide scale/metal interface, formation of interfacial pores and deteriorated scale adherence [17,18]. In contrast, in H_2/H_2O mixtures the growth process involved a certain extent of inward diffusion transport, whereby the scale growth rate increased but the scale adherence improved [19]. The effect of the atmosphere on the scale growth rate might change, depending on the presence of other alloying elements in the scale, e.g. Mn [14]. A Mn-containing model Ni-25Cr alloy showed a decreased oxidation rate in H_2/H_2O vs. Ar-O_2, i.e. the opposite effect compared to the Mn-free alloy [16].

The diffusion ionic transport in the chromia scales occurs predominantly at the oxide grain boundaries [20]. The transport properties of the chromia grain boundaries (GBs) affect the

overall oxidation kinetics and depend strongly on the oxide microstructure and especially on the GB chemistry [21]. Unfortunately, till now only limited publications with studies dealing with the grain boundary chemistry in the oxide scales on ferritic steels are available. Electron microscopy based techniques such as scanning and transmission electron microscopy (SEM/TEM) are conventionally used for the microstructure characterization of oxide layers [22–26]. These methods, however, exhibit limited analytical capabilities, especially when it comes to the analysis of low-concentrated solutes at low-sized and non-planar objects such as GBs. In most cases, only qualitative analysis is available, and very limited studies provided estimates on the amount of the grain boundary segregants [22,27].

In addition to SEM and TEM, atom probe tomography (APT) has recently started to be used for oxide scale analysis. APT can perform elemental analysis of a material in 3D with sub nanometer resolution and high sensitivity levels for all elements of the periodic table [28]. It has been successfully utilized in the recent years for the investigation of thermally grown oxide scales on steels [29–33] as well as on other alloy systems [34–39] and clearly demonstrated its unique strength in analysis of grain boundaries.

The present work investigates the effect of test gas compositions on the short-term high-temperature (800 ^{o}C) oxidation behavior of a high-Cr ferritic steel containing minor additions of Mn, Nb and Ti. This composition is similar to that of the commercially available steel Crofer 22 H [5], however with a low silicon content of 0.04 wt. %. The exposures were carried out in simulated SOC environments, i.e. Ar-O_2, Ar-H_2-H_2O and Ar-CO-CO_2 atmospheres. The oxidation kinetics obtained from thermogravimetry are combined with detailed oxide scale analysis using SEM, TEM and APT in order to reveal the interplay between oxidation properties, microstructural evolution and role of alloying elements in different oxidizing atmospheres. Special attention has been placed on the chromia scale as it forms first before becoming covered by a Cr/Mn-spinel layer under the given oxidation conditions [40] and hence, the microstructure of chromia is of crucial importance for the diffusion of oxygen anions and metal cations during oxide scale growth.

2. Experimental Procedures

A model, high-Cr ferritic steel with a nominal composition Fe-24Cr-0.5Mn-0.6Nb-0.2Ti-0.1La (at.%) was selected for the studies. The steel was manufactured by VDM Metals using vacuum melting. An ingot of about 10 kg was cast and subsequently hot rolled down to sheets of 2 mm thickness. Chemical analysis of the steel composition was performed by inductively-coupled plasma optical emission spectroscopy (ICP-OES) for metals and combustion analysis for C and N, the results are provided in Table 1.

Table 1. Chemical composition of the alloy as determined by ICP-OES for metals and combustion analysis for C and N (in at. %)*

Element	Fe	Cr	Mn	Nb	Ti	Al	Si	La	C	N
Content	base	23.58	0.52	0.66	0.17	0.02	0.04	0.06	0.05	0.07

*Additionally, the alloy contains B and S in concentrations <0.01 at. %.

Samples of dimensions 20 x 10 x 2 mm were machined for oxidation testing from the hot rolled sheet by laser cutting. All machined samples were ground down to a 1200 grit surface finish with SiC abrasive papers. Prior to high temperature exposure, the samples underwent ultrasonic cleaning with ethanol. Thermogravimetric tests were performed at 800 °C in three model gas compositions simulating SOC operating environments, namely Ar-20%O_2, Ar-4%H_2-4%H_2O and Ar-1%CO-1%CO_2 atmospheres, using a Setaram TG 92 microbalance. The oxygen partial pressures (pO_2) of these gases were determined from FACTSAGE software and the values are shown in Table 2. For easy reading, the test gas compositions were shortened as mentioned in Table 2, and these shortened designations will be used from here. Based on the pO_2 values, these atmospheres can be classified as high pO_2 (Ar-O_2) and low pO_2 (Ar-H_2-H_2O, Ar-CO-CO_2) gases. During the TG-test each sample was heated at a rate of 90 K/min, kept at 800 °C for 72 hours (exposure time), and subsequently cooled in the furnace at approximately 10 K/min.

The microstructure of the post-oxidation samples was examined by scanning electron microscopy (SEM) using a Zeiss Supra 50VP instrument (Carl Zeiss Microscopy GmbH, Germany). For cross-section SEM investigation, the samples were mounted in an epoxy resin. Prior to mounting, the samples were coated with an approximately 100 nm thick gold layer to provide the necessary electrical conduction, and subsequently electroplated with Ni using

a nickel sulphate ($NiSO_4$) solution. The electroplated Ni layer provides mechanical support for the oxide scale during further metallographic preparation, and enhances the contrast between the oxide scale and the mounting material under SEM observation.

Table 2. The partial pressures of oxygen for the used gas compositions at 800°C.

Gas composition (shortened designation)	**pO_2 (atm)**	**classification**
Ar-20%O_2 (Ar-O_2)	0.2	high pO_2
Ar-4%H_2-4%H_2O (Ar-H_2-H_2O)	4.3 x 10^{-19} *	low pO_2
Ar-1%CO-1%CO_2 (Ar-CO-CO_2)	3.6 x 10^{-19} *	

* calculated using FACTSAGE

TEM specimens were produced using a Zeiss Auriga cross beam focused ion beam (FIB) with a Ga^+ ion source (Carl Zeiss Microscopy GmbH, Germany). High resolution electron imaging was performed using a Zeiss Libra 200 transmission electron microscope (Carl Zeiss Microscopy GmbH, Germany) with an accelerating voltage of 200 kV. Elemental analysis was carried out by energy dispersive X-ray spectroscopy (EDS) using a X-Max 80 detector (Oxford Instruments, UK).

For APT investigations, a conventional lift-out method [41] was used for preparing APT specimens from the Cr_2O_3 region of the cross-sectional sample using a Helios Nanolab 650i dual beam FIB (Thermo Fisher Scientific, USA). The Cr_2O_3 scale lift-outs were prepared perpendicular to the oxide growth direction (parallel to the oxide scale surface) to increase the number of GBs in APT datasets, as Cr_2O_3 grains are textured (elongated) in the growth direction. APT measurements were conducted using a LEAP 4000X HR instrument (Ametek Inc., USA) operating in laser mode with laser pulse frequencies of 200-250 kHz, laser pulse energies in the range of 30-50 pJ and detection rate of 0.005 ions per pulse. The specimen temperature was maintained at 50 K for all measurements. At least three APT specimens/datasets were measured for each gas composition (see Supplementary Data). APT data reconstruction and analysis was done using the Integrated Visualization and Analysis

Software (IVAS™) package 3.6.14 (Ametek Inc.). The details of the reconstruction procedure are provided in the Supplementary Information of our previous publication [42].

3. Results

3.1 Oxidation kinetics

Figure 1a shows the thermogravimetric data acquired during isothermal oxidation in the model gas compositions at 800 °C for 72 hours of exposure. During oxidation, the weight gain by the sample exposed in high pO_2 (Ar-O_2) gas was lower compared to both low pO_2 gases (Figure 1a). Figure 1b shows the instantaneous "apparent" parabolic oxidation rate constant [43] as function of time ($k'_w(t)$) calculated by local fitting of the weight change data in Figure 1a assuming a parabolic rate law. The calculation procedure is described in reference [44]. From Figure 1b it is apparent that after approximately 10-hour exposure, the oxidation rates in low pO_2 gases become similar and after longer times tend to be even slightly lower than in the high pO_2 atmosphere.

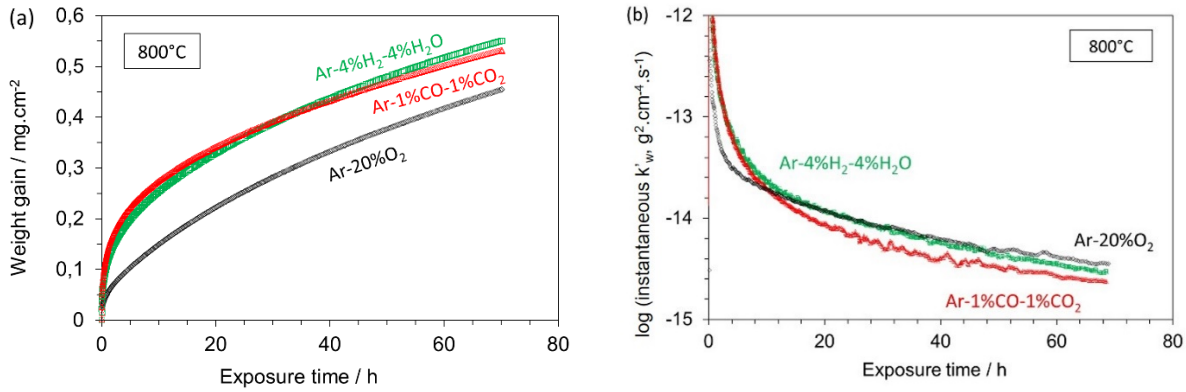

Figure 1 Thermogravimetric test results acquired during isothermal oxidation at 800 °C in SOC model test gases up to 72 hours of exposure: (a) weight gain as a function of exposure time and (b) instantaneous "apparent" parabolic rate constant $k'_w(t)$ as a function of exposure time. The error of the weight gain measurements is <1 µg/cm^2.

3.2 Electron Microscopy Analysis

Figure 2 depicts surface morphologies and cross sections of the oxidized samples imaged by SEM. In the high pO_2 environment (Ar-O_2), the surface oxide shows a globular morphology (Figure 2a), whereas in both low pO_2 gases (Ar-H_2-H_2O and Ar-CO-CO_2), a well-developed

plate-like morphology was observed (Figure 2b and 2c). Thus, the outer oxide scale formed in the high pO_2 is denser and more compact than those formed under low pO_2 conditions.

The cross-sectional analysis showed a duplex oxide scale consisting of outer spinel ($MnCr_2O_4$) and inner chromia (Cr_2O_3) for all gases, which was confirmed by XRD and Raman spectroscopy [15]. Under high pO_2, the chromia is denser, whereas in both low pO_2 gases the chromia is porous. Additionally, a Nb-rich oxide layer (with composition of $Nb(Ti,Cr)O_2$, see earlier work [15]for more details) was formed between metal and chromia, which is continuous in the case of low pO_2 gases but discontinuous at high pO_2. It is also observed from Figure 2d-2f, that the overall thickness of the oxide scale formed in Ar-O_2 is smaller than that of the scales formed in Ar-H_2-H_2O and Ar-CO-CO_2, in agreement with the TG-data shown in Figure 1a. The thickness of the chromia part of the scale is comparable in all test atmospheres. Additionally, an internal oxidation zone was observed after exposure in all specimens, being less pronounced in case of the samples exposed in the high pO_2 atmosphere (Figure 2d).

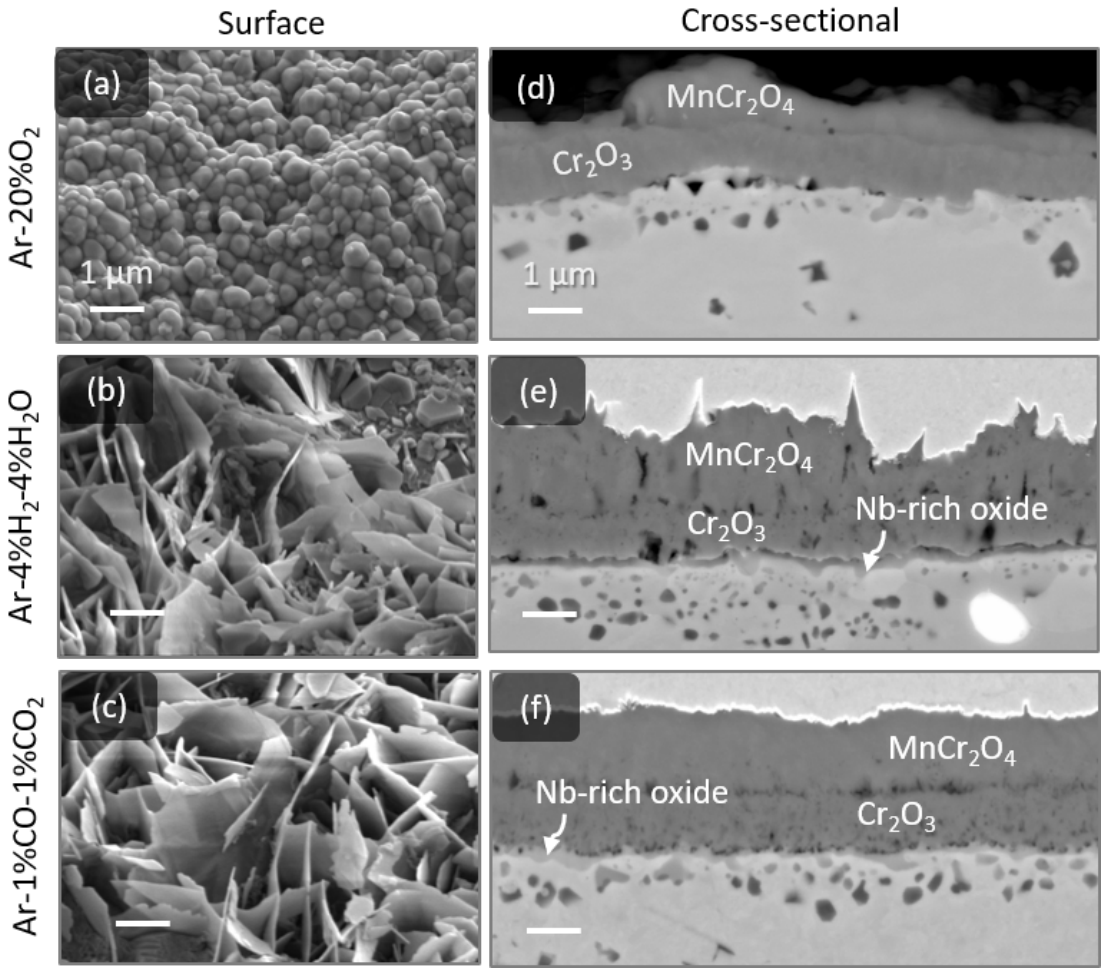

Figure 2 Surface morphology (left column) and cross section (right column) SEM micrographs of the samples exposed at 800 °C in Ar-O_2 (a, d); Ar-H_2-H_2O (b, e); and Ar-CO-CO_2 (c, f) for 72 hours. All micrographs are presented at the same magnification.

Figure 3 shows high-angular annual dark field (HAADF) STEM images of cross sections as well as STEM-EDS elemental maps of O, Cr, Nb, Ti and Mn in the oxide scale formed in Ar-O_2 (Figure 3a), Ar-H_2-H_2O (Figure 3b) and Ar-CO-CO_2 (Figure 3c). In Figure 3a, it can be seen that a discontinuous Nb-rich oxide layer is formed at the chromia-metal interface in Ar-O_2. Ti displayed the tendency to form internal oxide precipitates identified as TiO_2. Mn is found in the outer part as spinel and, locally, at the oxide-alloy interface as inner spinel islands.

Interestingly, in both low pO_2 atmospheres, chromia whiskers or platelets were formed on top of the Cr_2O_3 scale, penetrating into the surface spinel layer (as shown in the Cr-mappings in Figure 3). The Nb-rich oxide layer is continuous, consistent with the lower magnification images in Fig.2. This contrasts with the observations in high pO2 gas. Furthermore, no inner Mn-spinel could be observed in either Ar-H_2-H_2O or Ar-CO-CO_2, as confirmed by comparing with the Mn map in Fig.3.

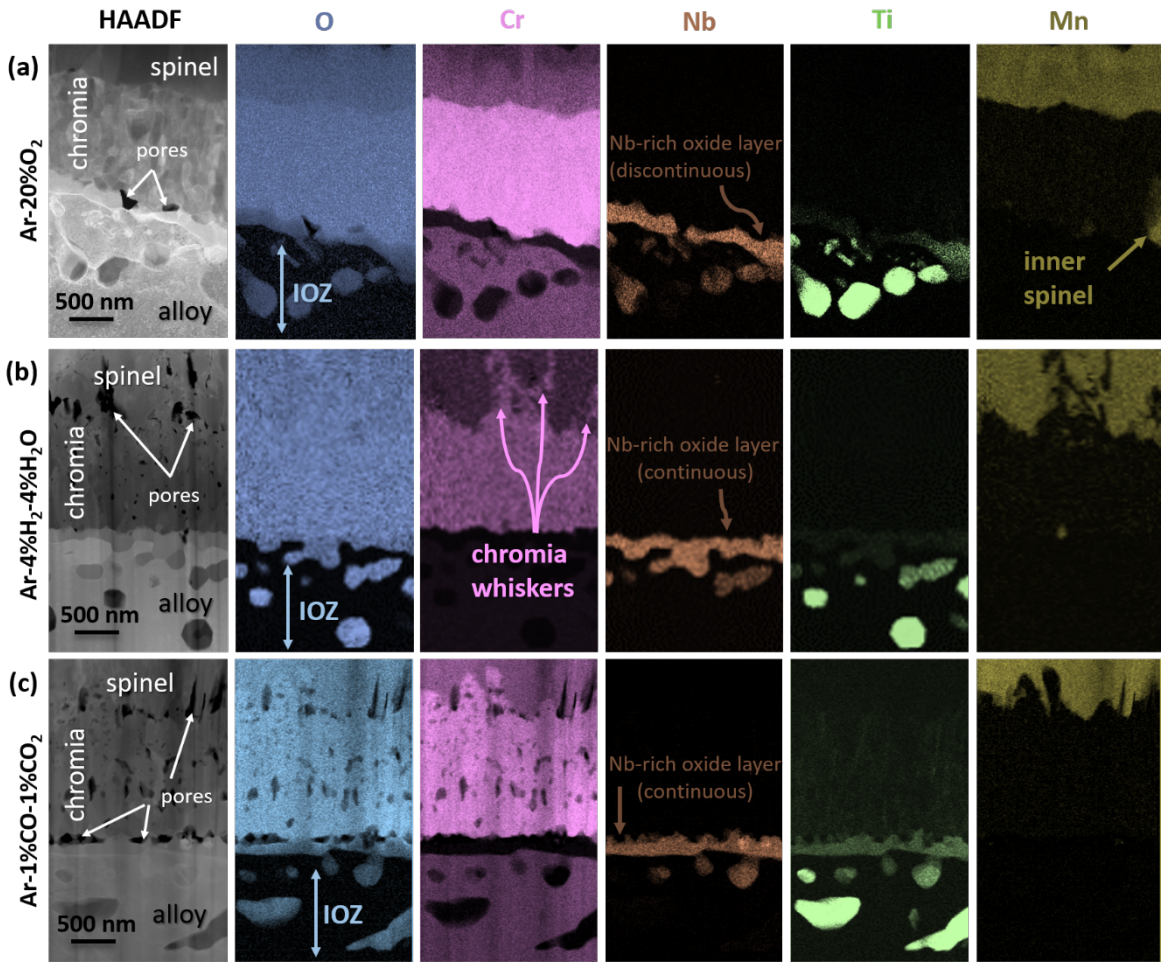

Figure 3 HAADF-STEM micrographs and corresponding STEM-EDS maps showing elemental distribution in the oxide scales formed at 800 °C during 72 hours of exposure in (a) Ar-O_2 and (b) Ar-H_2-H_2O and (c) Ar-CO-CO_2.

3.3 Atom Probe Tomography (APT) analysis of the chromia scale

3.3.1 Chromia scale in Ar-O_2

As mentioned above, grain boundaries are critical for the mass transport through the growing chromia scale. TEM does not possess the capability to resolve and quantify the GB chemistry at the level enabling an accurate and reliable comparison of the studied samples. For gaining detailed insights into the local composition of the Cr_2O_3 GBs formed in the SOC model gas compositions, APT was employed. In order to ensure a correct comparison of the oxidation behavior in different gas compositions, all APT specimens were prepared from the middle of the Cr_2O_3 scale.

Figure 4 shows APT analysis of the chromia scale formed in Ar-O_2 at 800 °C after 72 hours of exposure. The chromia bulk composition (averaged over grains and GBs) is displayed in Table 3. The relatively lower oxygen content compared to the nominal one is a typical APT artifact in oxide materials [45,46]. The APT data in Table 3 show the presence of Mn, Ti, Nb, Fe and Al with a sum amount of less than 1.5 at. %. However, as can be seen in Figure 4a, Ti, Nb and Mn show preferential segregation to chromia GBs. Additionally, doping of Ti, Mn and Fe into the chromia lattice can be seen from Table 3 as well as from the concentration profiles for minor elements (Figure 4b). The peak concentrations for minor elements like Ti, Nb, Mn and Fe at chromia GBs are 2.2, 1.2, 0.4 and 0.05 at% respectively.

Table 3 APT bulk composition (in at.%) analysis of Cr_2O_3 scales formed after 72 hours of exposure at 800°C in the three test gases. Ideal 'O' content of a stoichiometric Cr_2O_3 is 60 at.%.

Gas compositions	**O***	**Cr**	**Mn**	**Ti**	**Nb**	**Al**	**Fe**
Ar-O_2	56.4	42.2	0.36	0.66	0.13	0.03	0.13
Ar-H_2-H_2O	56.1	41.9	0.05	0.82	0.10	0.09	<0.01
Ar-CO-CO_2	56.1	43.1	0.03	0.54	0.05	0.01	<0.01

*Underestimation of oxygen content from the oxide materials is a typical APT artifact [45,46].

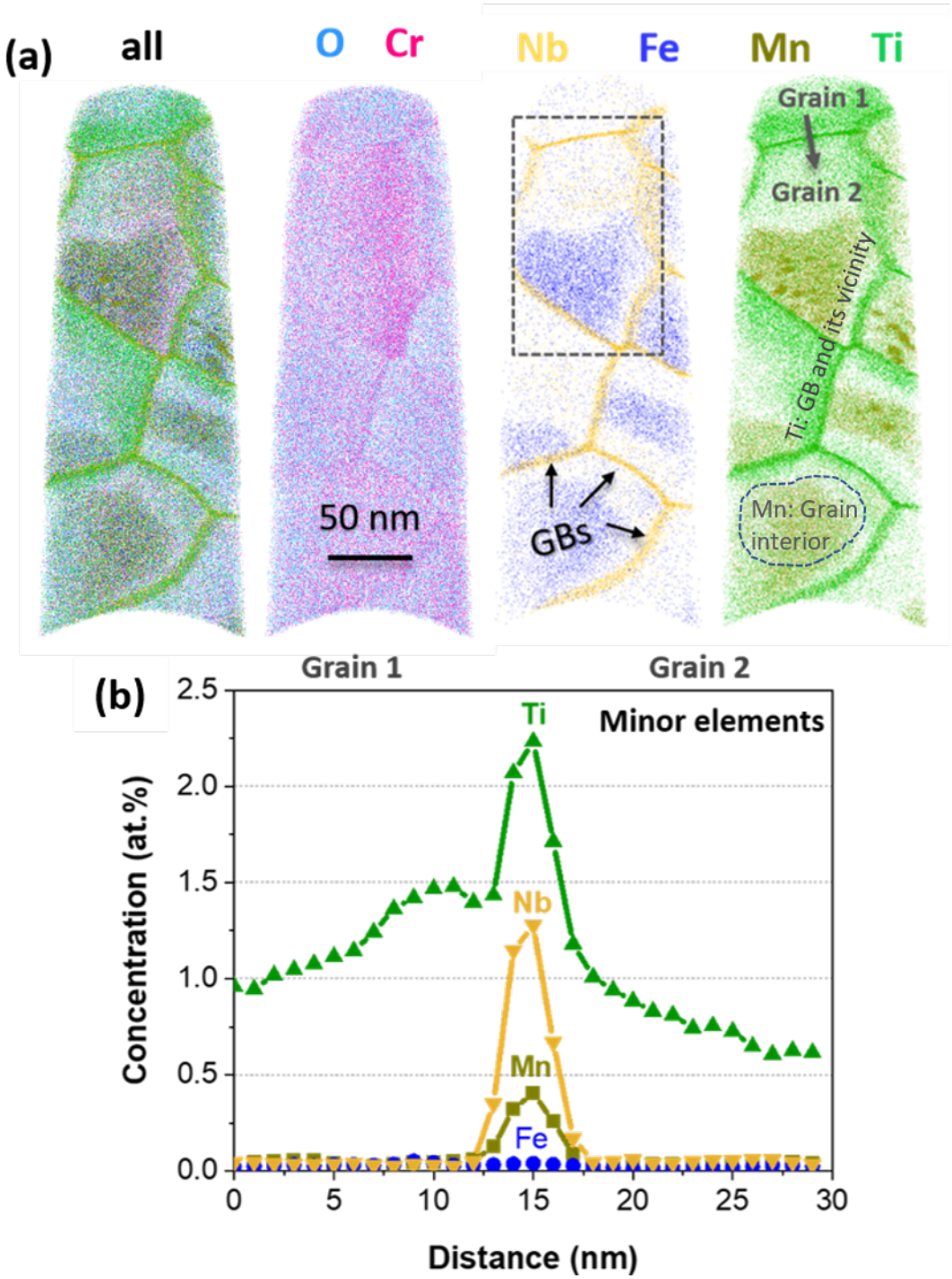

Figure 4 APT analysis of Cr_2O_3 scale formed during exposure in Ar-20%O_2 at 800 °C for 72 hours. (a) Atom maps of Cr_2O_3 showing the elemental segregation at grain boundaries. (b) GB concentration profiles between grains 1 and 2 for minor elements (Ti, Nb, Mn and Fe).

A small sub-volume containing a Mn-rich column inside a chromia grain was extracted from the dataset presented in Figure 4a and analyzed in more details in Figure 5a. Mn showed a clear tendency to form Mn-rich regions in the Cr_2O_3 grain interiors, which are additionally

enriched in Fe. The concentration profile in Figure 5b shows an inhomogeneous chemical distribution across the chromia grain, where the Mn concentration varies from almost zero on one side (extreme left) to a maximum of about 2.3 at. % (right side). However, the proximity histogram built across the Mn isoconcentration surfaces in Figure 6c shows the presence of high-Mn nanoregions with local concentration of about 8 at. %. Although this concentration is lower than ~14 at. % Mn in the stoichiometric Cr_2MnO_4 spinel, these Mn-rich nanoregions may be representing spinel nuclei, which later transform into the observed inner spinel inclusions (see Figure 3a).

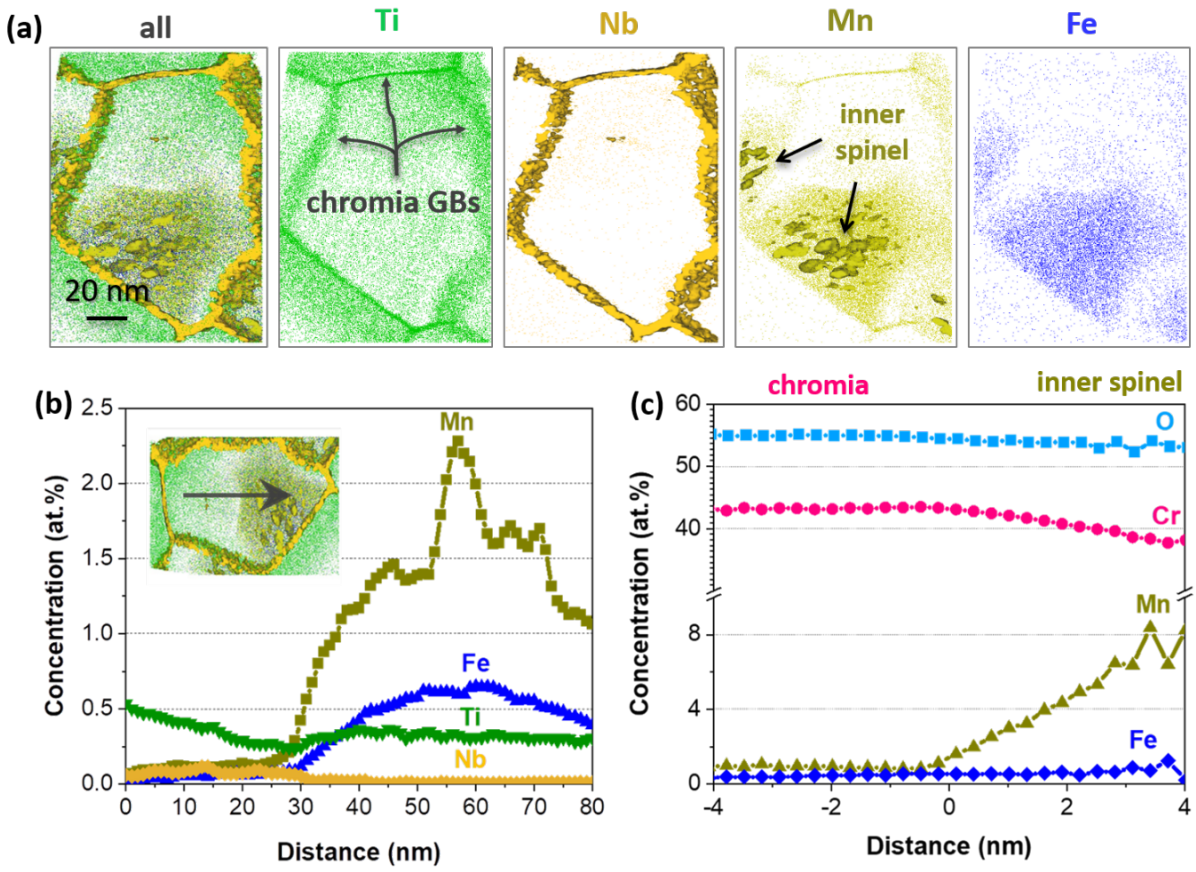

Figure 5 (a) APT elemental maps of chromia scale formed after exposure in Ar-20%O_2 at 800 °C for 72 hours decorated with Nb and Mn iso-concentration surfaces, (b) concentration profiles showing the variation in the chemical composition within a grain and (c) proximity histograms for the Mn-rich nanoprecipitates (inner spinel nuclei).

3.3.2 Chromia scale in Ar-H_2-H_2O

The atom maps of the chromia scale formed in Ar-H_2-H_2O, as shown in Figure 6, reflect the fine-grained nature of the chromia scale. This is evident through the segregation of minor alloying elements such as Ti, Nb, Mn and Al at GBs. In all samples, Ti is the only element that demonstrates notable solubility (approximately 0.5 at. %) within the chromia grains, while Nb exclusively segregates to grain boundaries. The bulk composition of the chromia scale indicates a total 0.82 at. % of Ti (see Table 3). The chromia scale has a relatively low amount of Mn (0.05 at.%), and nearly no Fe (<0.01 at.%) was detected. Si appears as an island-like segregation patterns randomly formed inside the chromia grains, at GBs and at triple junctions. This is in contrast to the chromia scale formed in Ar-O_2, where no Si segregation was observed.

The degree of GB segregation can be quantitatively shown by plotting concentration profiles across a chromia GB (see Figure 6b). The peak concentration at the GBs reaches approximately 2.5 at. % for Ti, 1.2 at. % for Nb and 0.25 at. % for Mn, which is close to the values observed in the high pO_2 gas (compare with Figure 4b). Al segregation is slightly displaced from other segregating elements, which might occur due to space charge distribution at the GB plane by heavier cations like Nb, Ti, Mn and Si [15].

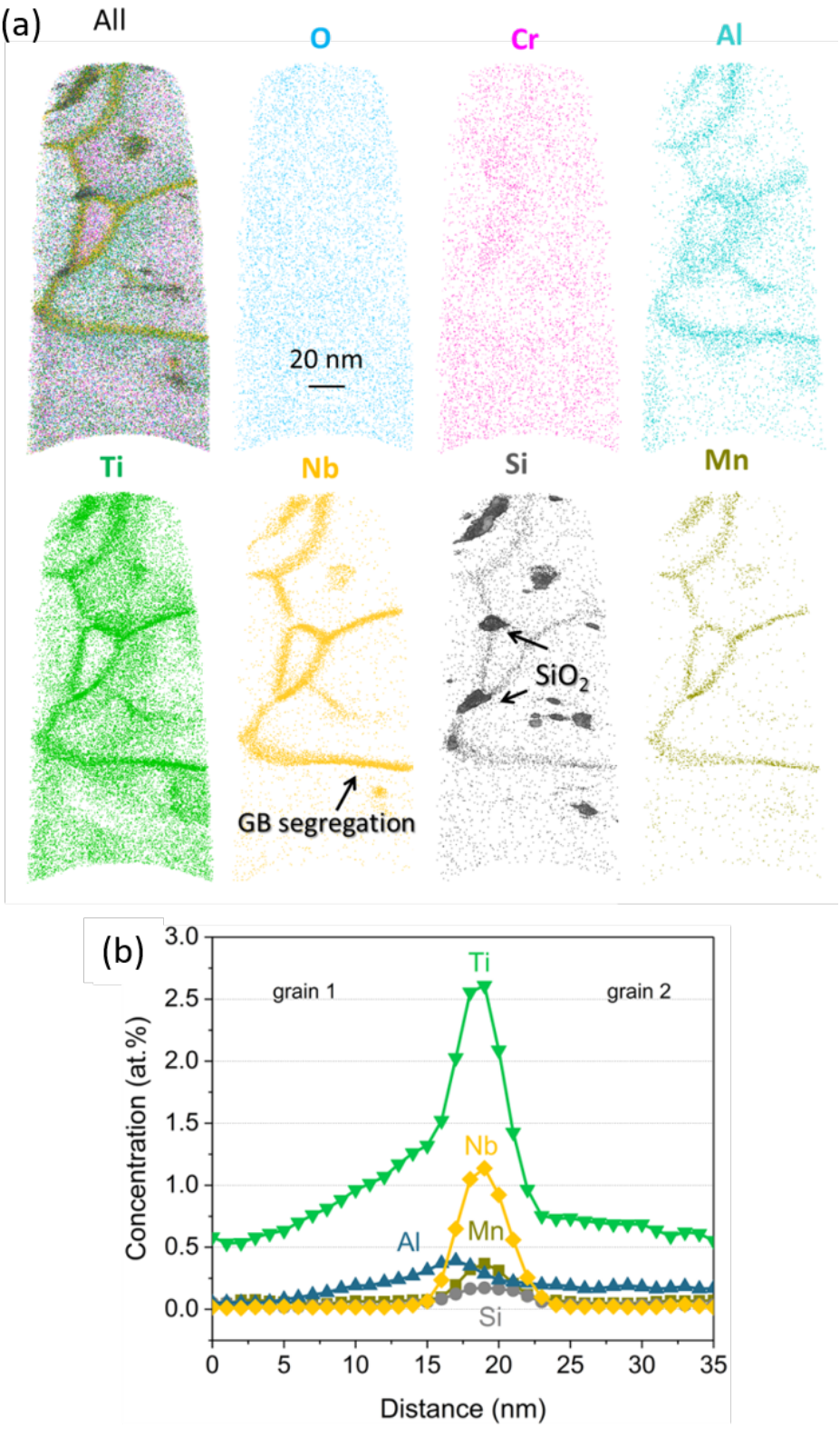

Figure 6 (a) APT elemental maps of the chromia scale after 72 hours isothermal oxidation at 800 °C in Ar-H_2-H_2O. (b) concentration profiles across chromia GBs for minor alloying elements.

3.3.3 Chromia scale in Ar-CO-CO_2

Figure 7 shows the results of the APT analysis of the chromia scale formed in Ar-CO-CO_2. The APT dataset reveals a network of grains and GBs, including a triple junction, illustrating the fine-grained nature of the chromia scale.

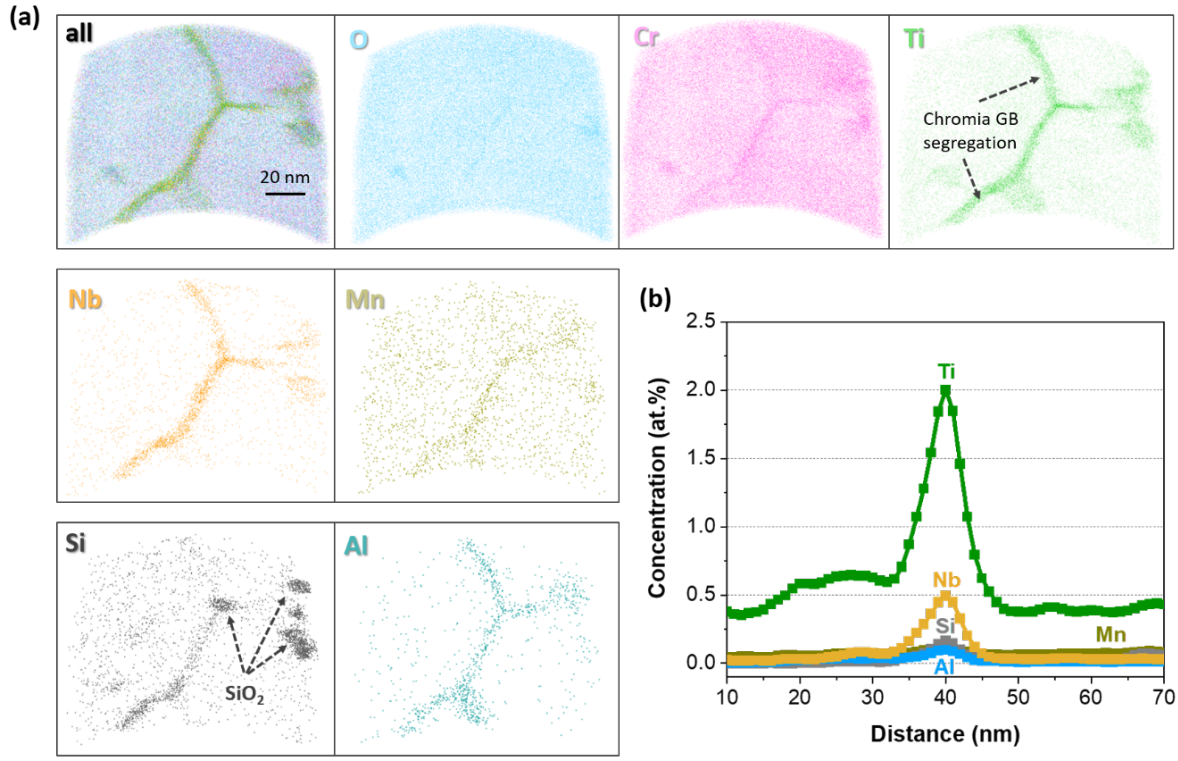

Figure 7 (a) Elemental APT maps of the chromia scale formed after 72 hours isothermal oxidation at 800 °C in Ar-CO-CO_2 and (b) concentration profiles across a chromia grain boundary.

Ti, Nb, Mn and Al segregate at chromia GBs, whereas Si shows an island-like segregation pattern, very similar to that of the chromia scale formed in Ar-H_2-H_2O. The GB segregation behavior of minor alloying constituents as shown in Figure 7b is quantitatively similar to those found in the scale formed in the other gas compositions, except a broader range of GB segregation, which is due to curved nature of GBs in Ar-CO-CO_2. It is worth mentioning that carbon was not detected in any part of the chromia scale, at least above the sensitivity limit of the APT analysis (~10 ppm).

4. Discussion

4.1 Oxide scale volatilization

Before discussing the obtained results, a remark should be made with respect to the mechanisms of oxide scale growth. Considering high-temperature exposure of chromia-forming alloys and coatings, volatilization of the scale due to reaction with the environment cannot, in general, be excluded. Thermodynamically, the volatile species in equilibrium with the chromia scale possessing the highest vapor pressure are CrO_3 and $CrO(OH)_2$. For exposure in Ar-O_2, only minor evaporation can be expected based on the fact that the partial pressure of CrO_3 at 800 °C is extremely low, in the order of 10^{-10} atm [47]. In the H_2/H_2O-atmosphere the oxygen activity is very low, consequently very low partial pressure of CrO_3 as well as $CrO(OH)_2$ are expected (in the order of 10^{-19} atm according to Niewolak, et al [14]). Therefore, under the presently used experimental conditions (gases, temperature and time) the scale evaporation can be neglected, and only reaction processes involving formation of solid-state products are considered.

In the following discussion we first correlate the oxidation kinetics with the overall scale composition including chromia and spinel parts. Subsequently, the properties of the formed chromia scales including the oxide grain size, segregation behavior at the oxide grain boundaries and porosity formation and their influence on the scale transport processes are discussed.

4.2 Correlation between the oxidation kinetics and oxide scale structure

The instantaneous oxidation rates at 800°C of the studied Nb, Ti and Mn containing model ferritic high-Cr steel are initially higher in H_2/H_2O and CO/CO_2 than in Ar-O_2. After approximately 10 hours exposure the oxidation rates become similar and after longer times even slightly lower rates are found in the lower pO_2 test gases compared to Ar-O_2 (Figure 1b).

As mentioned in the introduction, pure chromia scales on Cr-metal as well as on Cr-rich, binary Ni and Fe based alloys exhibit higher growth rates in H_2/H_2O gas mixtures than in O_2 atmosphere. Niewolak et al. [14] studied the time-dependent oxidation behaviour at 800°C of the commercial ferritic steel Crofer 22H with a similar basic composition (but a higher Si content) in dry synthetic air and Ar-H_2-H_2O. They found that the steel initially formed a

chromia scale growing faster in the low pO_2 test gas. A similar situation is likely to have occurred in the low pO_2 environments of the present study. It should be mentioned that the absolute values of mass changes measured in [14] are substantially lower than those observed in the present work. This difference can be explained by differences in the compositions of the steels, in particular a much lower content of Si in the presently studied steel compared to Crofer 22H. As explained in our previous work [15], minor Nb addition to the steel increases the growth rate of chromia by a GB segregation effect. In contrast in Crofer 22H Nb is tied up in a Si-containing Laves phase, which suppresses the Nb effect on chromia growth rate [7].

From the SEM (Figure 2) and TEM (Figure 3) results, it is obvious that the thickness of the chromia parts of the scales formed in all three studied atmospheres after 72h is comparable in spite of substantial differences in the initial oxidation rates. From Figure 2 it can be seen that the thickness of the spinel layer is greater by around a factor of two in the low pO_2 test gases compared to that formed in the high pO_2 gas, which is in principle in agreement with the higher mass changes in the former test gases (compare with Figure 1a). The full coverage of the chromia scale by the spinel is commonly found after a certain exposure time, i.e. after sufficient Mn incorporation into the scale occurred. The spinel morphology is clearly different between the two types of test gases (high and low pO_2 gases). Whisker or blade like spinel morphology in H_2/H_2O atmospheres was associated with the thermodynamic stability of stoichiometric $MnCr_2O_4$ type spinel in this atmosphere, contrary to the $(Mn,Cr)_3O_4$ type spinel with blocky morphology found in air [14]. The formation of different types of spinel phases in high pO_2 (Ar-O_2) and low pO_2 (Ar-H_2-H_2O and Ar-CO-CO_2) gases respectively are confirmed by Raman spectroscopy measurements of the oxide scales on the studied model steel as has been presented elsewhere [15]. In the stoichiometric spinel, transport of Cr and Mn is virtually limited to grain boundaries whereas in the $(Mn,Cr)_3O_4$, lattice transport additionally occurs [14,48] in the low pO_2 gases might be attributed to fast grain boundary transport of Mn and Cr contrary to volume diffusion predominant in the $(Mn,Cr)_3O_4$ type.

The present results obtained for the model Crofer 22 type steel with Mn, Ti and Nb additions in CO/CO_2 test gas are very similar to those in H_2/H_2O. This concerns the changes in the instantaneous oxidation rate as function of time (compare Figure 1b), the morphologies of

the outer spinel layer (Figure 2 b,c), the thickness of the individual oxide layers as well as the internal oxidation zones. Based on the observations inB the present work in CO/CO_2 atmosphere it can be argued that the morphological and growth rate differences in the spinel and chromia formation are related mainly to differences in oxygen activity in the atmosphere, rather than to the presence of particular gas species, such as H_2 or H_2O.

This non-trivial time dependency of the oxidation rate is in good qualitative agreement with the observations by Niewolak et al. [14], who proposed that a strong decrease in the instantaneous k_p in the H_2/H_2O-atmosphere can be correlated with the formation of an outer spinel layer. Since the spinel grows on top of the already existing chromia layer, it requires Mn transport through chromia, so that the microstructure and/or GB chemistry of the chromia become of key importance and therefore will be discussed in the subsequent sections.

4.3 Grain size considerations for chromia scale growth

It is known that for Cr_2O_3 at 800°C, the diffusion via GBs is much faster than the lattice/bulk diffusion [20]. Therefore, Cr_2O_3 GB transport plays a significant role in the oxidation process and is expected to be rate-determining. The total mass transport through GBs is controlled by both the elemental diffusivity and the density of the GB network, determining the number of fast diffusion paths per unit area. From Figure 8, it can be seen that the chromia grains formed in the high pO_2 gas (Ar-O_2) are finer than those formed in the low pO_2 gases, and the GB network density is higher. This should provide more diffusion paths and hence increase total GB diffusion fluxes resulting in faster oxidation. However, the opposite effect was observed in this study using thermogravimetry, i.e. the lowest weight gain and the thinnest spinel were observed with smaller Cr_2O_3 grains formed in Ar-O_2, whereas the thickness of chromia is comparable in all three test gases after 72 hours. The observation of a fine grained microstructure of Cr_2O_3 formed in Ar-O_2 is different from that made in model chromia forming systems e.g. pure Cr [49] or binary Ni-Cr alloys [14]. The latter studies revealed that chromia scales formed in O_2 were coarser grained compared to those formed in H_2/H_2O. A different dependency of the chromia grain size on the atmosphere observed in the present work may be related to the presence of segregating elements, e.g. Ti, Mn and/or Nb or Si, which could

potentially hinder grain growth. It is worth mentioning that the pure Cr metal [49] and binary NiCr alloys [14] without any additions of Ti, Mn, Nb and/or Si, highlighting the absence of these elements in those studies.

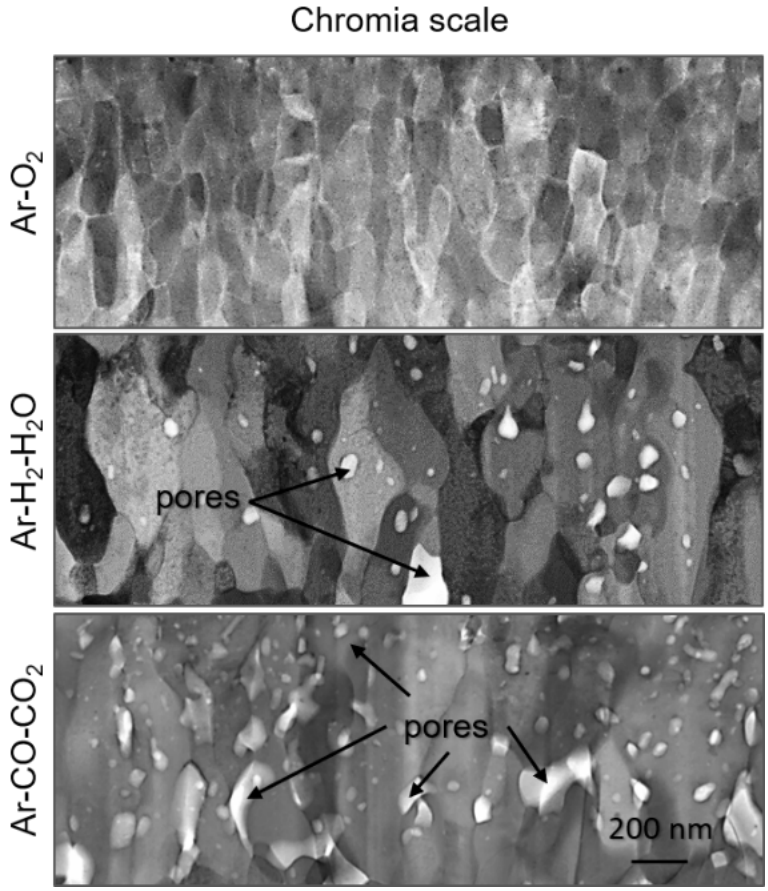

Figure 8 Bright field (BF) TEM micrographs depicting chromia microstructure formed in SOC model gas compositions during isothermal oxidation at 800 °C for 72 hours. All micrographs are presented at the same magnification.

4.4 Grain boundary segregation and its effect on Cr_2O_3 scale growth

The permeability of chromia GBs for metal cations (outward diffusion) or oxygen anions (inward diffusion) depends on their structure and chemistry, which may be directly influenced by GB segregation of other alloying constituents. It is observed from APT that the minor alloy constituents Mn, Ti and Nb segregate at Cr_2O_3 GBs. From the theory of Wagner-Hauffe, the doping of Cr_2O_3 lattice by the substitution of cations of higher oxidation state like $Nb^{4+/5+}$ and Ti^{4+} results in an increase in the concentration of chromium vacancies (V_{Cr}) or oxygen interstitials (O_i) whereas addition of cations of lower oxidation state like Mn^{2+} can in turn lead

to formation of oxygen vacancies (V_O) or Cr-interstitials [50]. This effect is popularly known as "aliovalent" substitution [51]. As derived in our previous work [15], the sum amount of segregating species at the chromia GBs exceeds a monolayer GB coverage in the case of Ar-H_2-H_2O atmosphere. Based on the approximately similar segregation activities of Ti, Nb and Mn in all gases in the present work, as evidenced from concentration profiles in Figs. 4-7, the same conclusion can be drawn here as well. Such a considerable segregation is expected to alter the microstructure and properties of the grain boundaries, so that GB structure and transport properties become very different from those of pure chromia. One of the important findings of the present study is that the segregation levels of all aliovalent impurities (Mn, Ti and Nb) at chromia GBs are quantitatively similar in all three test gases.

Formation of discrete silica particle and minor Si segregation was observed at the chromia grain boundaries of the scales formed in the low pO_2 gases but not in the high pO_2 gas (compare Figs 4, 6 and 7). The exact reason for this observation as well as its possible impact on the transport processes in the scale are not understood at the moment. Possibly, incorporation of Si into the chromia scale in the low pO_2 gases can be facilitated by enhanced internal oxidation of Si in the initial stages of exposure combined with a stronger inward scale growth. Promotion of internal oxidation during exposure in H_2/H_2O atmospheres compared to dry O_2 exposure was found in several ferritic materials [52]. The examples include internal oxidation of Cr in Fe-Cr alloys as well as enhanced internal oxidation of Zr in alumina forming FeCrAl-type alloys [53]. Thus, in the present work it is possible that Si internal oxidation had occurred in the beginning of exposure to the low pO_2 test gases. At later stages these Si-particles became embedded and Si distributed along the grain boundaries of the partially inwardly growing [14] chromia scales. The absence of Si segregation at GBs of chromia formed in the high pO_2 gas might be related to less pronounced initial Si internal oxidation and to less significant inward scale growth compared to those in the low pO_2 gases.

No carbon was detected in the chromia scale using APT and no internal carburization was observed in the studied model steel exposed to the Ar-1%CO-1%CO_2 atmosphere. Nguyen et al. [29] oxidized a Fe-20%Cr binary model alloy at 650°C and 818°C in a Ar-20%CO_2 atmosphere. Using APT the authors found Fe-Cr-spinel and carbon at the chromia grain boundaries and using TEM they also found internal carburization beneath the chromia scale.

The absence of carbon at the chromia grain boundaries in the present study might be related to low thermodynamic activity of carbon (a_C) in Ar-1%CO-1%CO_2 atmosphere compared to Nguyen's work. They also suggested that presence of Si at the grain boundaries of a chromia scale formed on Fe-20Cr-based, Si-containing model alloy in Ar-CO_2 at 650°C suppressed carbon penetration through the scale. In the present work, only minor Si-segregation to the chromia GBs was observed and it is unlikely that it plays a major role in suppressing carburization of the studied ferritic steel during exposure in the CO/CO_2 test gas, but further studies are required to verify this assumption.

4.5 Formation of pores and its role in the chromia scale growth

Figure 8 indicates that a dense chromia scale formed in Ar-O_2, whereas the scales formed in the low pO_2-gases exhibit noticeable porosity. The porosity in the Ar-H_2-H_2O atmosphere is slightly less pronounced compared to that in the Ar-CO-CO_2 gas, despite similar pO_2 levels. The presence of porosity may contribute to the observed differences in oxidation rates among the studied gases. This is because diffusion through the oxide scale can occur partially through the volumes and walls of the pores, which can provide faster diffusion pathways compared to solid-state diffusion alone, including grain boundaries. The extent of this process can be further enhanced if the pores are partially interconnected [54], resulting in significantly shortened diffusion paths through the solid phase. However, it should be noted that direct proof of this phenomenon requires the development of a dedicated experimental approach, as the current used analytical techniques do not provide conclusive evidence.

Formation of porosity was shown by Michalik et al. [49] to occur during oxidation of pure Cr at 1000 and 1050°C in Ar-4H_2-2%H_2O atmospheres, contrary to exposures in Ar-20%O_2, where dense chromia scales were observed. The proposed mechanism of porosity formation was analogous to that proposed by Rahmel and Tobolski [55] and Fuji and Meussner [56]. Formation of the pores was initiated at the oxide metal interface. Considering low oxygen activities at that location, the oxygen partial pressure within the pore should be very low, thereby enabling a negligibly small oxygen flux. It was proposed that oxygen was transported over the pore volume as H_2O-molecule and upon reaction with Cr, H_2 was transported back to the upper pore surface forming H_2O thereby providing a "bridge" for rapid oxygen

transport. As the chromia scale grows to some extent inward, the interfacial pores effectively move to the outer part of the scale. Such a mechanism could be considered to explain the pore formation in the H_2/H_2O gas. A similar bridge mechanism can be generally proposed to apply in the case of Ar-CO-CO_2 gas [55], with CO-CO_2-reaction providing a "bridge" for rapid oxygen transport. As mentioned above, no carbon was detected by APT studies within the chromia scale. However, the bridge mechanism implies the presence of carbon only in the gas entrapped within the pores. Moreover, the C incorporation into the chromia scale had likely occurred during the early oxidation and stopped at later stages. The coverage of the chromia surface with $MnCr_2O_4$ was observed by Niewolak et al. [14] to reduce the scale growth rate on the ferritic steel Crofer 22H in the H_2/H_2O-test gas compared to that in air. Apparently, the outer spinel layer prevents incorporation of H-containing species into the inner chromia. Based on this observation, one may argue that the top spinel should have a similar effect in CO/CO_2-atmospheres suppressing incorporation of carbon containing gas species into the chromia scale.

Considering the above discussion, the apparent discrepancy mentioned in section 4.1 between the scale composition, microstructure and instantaneous oxidation rates measured by thermogravimetry at 72 hours exposure in the studied test gases can be elucidated. The growth rates of the oxide scales in the low pO_2 test gases are initially high due to enhanced oxygen transport through the fine porosity within the chromia scale according to the Rahmel and Tobolsky (H_2/H_2O respectively CO/CO_2 bridge) mechanism. After some time, the chromia scales are covered with the $MnCr_2O_4$ spinel, which suppresses incorporation of hydrogen and carbon containing gas species into the chromia scale, thereby reducing its growth rate. The growth rate of stoichiometric $MnCr_2O_4$ is initially fast due to short circuit diffusion of Mn and Cr at the grain or twin boundaries of the chromia scale. At later stages depletion of Mn in the steel occurs and the Mn-incorporation into the scale ceases resulting in a decreased growth rate of the spinel.

In contrast to the low pO_2 gases, the dense chromia scale formed in Ar-O_2 initially exhibits a lower growth rate. However, over time, the chromia scale growth rate increases, developing a fine grain structure. On top of this, non-stoichiometric $(Mn,Cr)_3O_4$ spinel forms which results in the introduction of vacancies into the chromia scale. These vacancies facilitate the diffusion

of oxygen and other reactive cationic species through the chromia scale, allowing for a faster overall reaction rate of the studied ferritic steel. Consequently, at even longer exposure times than those addressed in the present work, the thickness of both the chromia and spinel sublayers formed in Ar-O_2 can be expected to exceed those formed in Ar-H_2-H_2O and Ar-CO-CO_2. The latter expectation is supported by observation in [14] with Crofer 22H exposed up to 10000 hours in H_2/H_2O and synthetic air.

Effect of Lanthanum: Insights from the nanoscale investigation

In previous studies, the influence of La as a reactive element on the adherence of oxide scales or oxidation rate in high-Cr steels was noted [57]. The observed effects were generally positive. Several explanations were proposed to account for the reactive element effect: (1) segregation of La within the oxide scale, directly influencing the growth process, (2) segregation of La at the metal-oxide interface, leading to alterations in adhesion properties, and (3) the ability of La to bind detrimental impurities, particularly sulphur, within the cast alloy.

To directly investigate the first two assumptions, APT analysis was conducted on three different gas compositions as reported earlier. It was anticipated that the detection of La or LaO_x ions of varying charge states in the mass spectra would be straightforward, as there would be no overlap with other ions. However, despite the detection sensitivity of APT reaching down to 10 ppm, no traces of La were observed in any region of the oxide scale or at the metal-oxide interface. This observation appears to contradict the proposed mechanisms (1) and (2) for the studied alloys, which suggest direct involvement of La in the oxidation process. The absence of La detection by APT hints that metallic La may have undergone oxidation during the casting process and could potentially exist in the form of oxide particles deep within the bulk alloy, rather than being present in the vicinity of the oxide scales on the surface.

5. Conclusions

The short time oxidation behavior at 800 °C of a high-Cr ferritic steel was studied in gases simulating solid oxide cell environments including a high pO_2 Ar-20%O_2, and low pO_2 Ar-4%H_2-

4%H_2O and Ar-1%CO-1%CO_2. The key findings of the investigation using thermogravimetry, SEM, TEM and APT can be summarized as follows:

1. The overall oxidation rate of the samples exposed in the low pO_2 gases is initially higher compared to that in the high pO_2 gas. After about 10 hours of exposure, the instantaneous oxidation rates in the low pO_2 gases become comparable and later tend to be even slightly lower than that in the high pO_2 gas.
2. After 72 hours, the oxide scales in the studied gas compositions display a duplex microstructure with an outer layer of Mn/Cr-spinel and an inner chromia layer. At the oxide-metal interface, a thin layer of Nb(Cr,Ti)O_2-rich rutile-type oxide forms, which is nearly continuous under low pO_2 gases but discontinuous under high pO_2 gases.
3. The compositions and microstructures of the outer scales in both studied low pO_2 gases are very similar, featuring whisker and blade type morphology of stoichiometric $MnCr_2O_4$, contrary to an equiaxed non-stoichiometric $(Mn,Cr)_3O_4$ grown in the high pO_2 gas.
4. TEM investigations of the chromia subscale revealed formation of dense oxide with a fine grain structure in the high pO_2 atmosphere. Exposure in the low pO_2 atmospheres results in formation of slightly coarser grained chromia scales containing substantial porosity.
5. APT analysis revealed that Mn, Ti and Nb segregate to the Cr_2O_3 grain boundaries in similar amounts across all gas compositions. This suggests that the differences in growth rate and morphology between the oxide scale formed in Ar-O_2 and those in Ar-H_2-H_2O and Ar-CO-CO_2 are not influenced by variations in grain boundary transport properties. Moreover, under high pO_2 conditions (Ar-O_2 gas), significant accumulation of Mn and Fe impurities inside Cr_2O_3 grains occurs, which is not observed in the low pO_2 gases (Ar-H_2-H_2O and Ar-CO-CO_2). Additionally, a minor discontinuous silicon segregation to the Cr_2O_3 grain boundaries is observed in the low pO_2 gases.
6. The fast-initial oxidation rate of the steel in the low pO_2 gases is likely related to faster oxygen transport assisted by hydrogen and respectively carbon containing species in the porous chromia scales and rapid growth of outer stoichiometric $MnCr_2O_4$. At longer exposure times, complete spinel coverage combined with Mn-depletion in the

alloy slows down the growth of chromia effectively reducing the overall oxidation rate below that in the high pO_2 test gas. The formation of $Nb(Cr,Ti)O_2$ at the oxide/metal interface is not believed to influence the growth rate of the chromia and spinel parts of the scale.

Acknowledgements

The authors acknowledge their colleagues Mr. Heiko Cosler and Dr. Egbert Wessel from the Institute of Energy and Climate Research (IEK-2) of Forschungszentrum Jülich GmbH for performing the thermogravimetry experiments and SEM analyses respectively. A part of the presented investigations was carried out at RWTH Aachen University within the framework of the Collaborative Research Centre SFB1120-236616214 “Bauteilpräzision durch Beherrschung von Schmelze und Erstarrung in Produktionsprozessen” and funded by the Deutsche Forschungsgemeinschaft e.V. (DFG, German Research Foundation). The sponsorship and support are gratefully acknowledged.

References

[1] S.C. Singhal, K. Kendall, High-temperature Solid Oxide Fuel Cells: Fundamentals, Design and Applications, Elsevier, 2003. https://doi.org/10.1016/B978-1-85617-387-2.X5016-8.

[2] R. Peters, M. Frank, W. Tiedemann, I. Hoven, R. Deja, N. Kruse, Q. Fang, L. Blum, R. Peters, Long-Term Experience with a 5/15kW-Class Reversible Solid Oxide Cell System, J. Electrochem. Soc. 168 (2021) 014508. https://doi.org/10.1149/1945-7111/abdc79.

[3] K. Kendall, M. Kendall, High-Temperature Solid Oxide Fuel Cells for the 21st Century, Elsevier, 2016. https://doi.org/10.1016/C2011-0-09278-5.

[4] V. Shemet, J. Piron-Abellan, W.J. Quadakkers, L. Singheiser, Metallic Materials in Solid Oxide Fuel Cells, in: Fuel Cell Technol. State Perspect., Springer-Verlag, Berlin/Heidelberg, n.d.: pp. 97–106. https://doi.org/10.1007/1-4020-3498-9_9.

[5] L. Singheiser, P. Huczkowski, T. Markus, W.J. Quadakkers, High Temperature Corrosion Issues for Metallic Materials in Solid Oxide Fuel Cells, in: Shreir's Corros., Elsevier, 2010: pp. 482–517. https://doi.org/10.1016/B978-044452787-5.00024-X.

[6] B. Kuhn, M. Talik, L. Niewolak, J. Zurek, H. Hattendorf, P.J. Ennis, W.J. Quadakkers, T. Beck, L. Singheiser, Development of high chromium ferritic steels strengthened by intermetallic phases, Mater. Sci. Eng. A. 594 (2014) 372–380. https://doi.org/10.1016/j.msea.2013.11.048.

[7] J. Froitzheim, G.H. Meier, L. Niewolak, P.J. Ennis, H. Hattendorf, L. Singheiser, W.J. Quadakkers, Development of high strength ferritic steel for interconnect application in SOFCs, J. Power Sources. 178 (2008) 163–173. https://doi.org/10.1016/j.jpowsour.2007.12.028.

[8] VDM Metals, VDM ® Crofer 22 APU Data Sheet, (2021). https://www.vdm-metals.com/fileadmin/user_upload/Downloads/Data_Sheets/Data_Sheet_VDM_Crofer_22_APU.pdf.

[9] L. Niewolak, F. Tietz, W.J. Quadakkers, Interconnects, in: High-Temperature Solid Oxide Fuel Cells 21st Century, Elsevier, 2016: pp. 195–254. https://doi.org/10.1016/B978-0-12-410453-2.00007-5.

[10] VDM ® Crofer 22 H Data Sheet, Data Sheet VDM Crofer 22 H. (n.d.).

https://www.vdm-metals.com/fileadmin/user_upload/Downloads/Data_Sheets/Data_Sheet_VDM_Crofer_22_H.pdf.

[11] L. Blum, Q. Fang, L.G.J. de Haart, J. Malzbender, N. Margaritis, N.H. Menzler, R. Peters, SOC Development at Forschungszentrum Jülich, ECS Trans. 78 (2017) 1791–1804. https://doi.org/10.1149/07801.1791ecst.

[12] S. Linderoth, P. V. Hendriksen, M. Mogensen, N. Langvad, Investigations of metallic alloys for use as interconnects in solid oxide fuel cell stacks, J. Mater. Sci. 31 (1996) 5077–5082. https://doi.org/10.1007/BF00355908.

[13] T. Brylewski, M. Nanko, T. Maruyama, K. Przybylski, Application of Fe–16Cr ferritic alloy to interconnector for a solid oxide fuel cell, Solid State Ionics. 143 (2001) 131–150. https://doi.org/10.1016/S0167-2738(01)00863-3.

[14] L. Niewolak, D.J. Young, H. Hattendorf, L. Singheiser, W.J. Quadakkers, Mechanisms of Oxide Scale Formation on Ferritic Interconnect Steel in Simulated Low and High pO2 Service Environments of Solid Oxide Fuel Cells, Oxid. Met. 82 (2014) 123–143. https://doi.org/10.1007/s11085-014-9481-8.

[15] A. Vayyala, I. Povstugar, T. Galiullin, D. Naumenko, W.J. Quadakkers, H. Hattendorf, J. Mayer, Effect of Nb Addition on Oxidation Mechanisms of High Cr Ferritic Steel in Ar–H2–H2O, Oxid. Met. (2019). https://doi.org/10.1007/s11085-019-09933-x.

[16] J. Zurek, D.J. Young, E. Essuman, M. Hänsel, H.J. Penkalla, L. Niewolak, W.J. Quadakkers, Growth and adherence of chromia based surface scales on Ni-base alloys in high- and low-pO2 gases, Mater. Sci. Eng. A. 477 (2008) 259–270. https://doi.org/10.1016/j.msea.2007.05.035.

[17] N. Shaigan, D.G. Ivey, W. Chen, Metal–Oxide Scale Interfacial Imperfections and Performance of Stainless Steels Utilized as Interconnects in Solid Oxide Fuel Cells, J. Electrochem. Soc. 156 (2009) B765. https://doi.org/10.1149/1.3116252.

[18] R.P. Oleksak, M. Kapoor, D.E. Perea, G.R. Holcomb, The role of metal vacancies during high-temperature oxidation of alloys, (2018) 1–8. https://doi.org/10.1038/s41529-018-0046-1.

[19] D.J. Young, J. Zurek, L. Singheiser, W.J. Quadakkers, Temperature dependence of oxide scale formation on high-Cr ferritic steels in Ar-H_2-H_2O, Corros. Sci. 53 (2011)

2131–2141. https://doi.org/10.1016/j.corsci.2011.02.031.

[20] D.J. Young, High Temperature Oxidation and Corrosion of Metals, 2015. https://doi.org/10.1017/CBO9781107415324.004.

[21] W. Kingery, Segregation phenomena at surfaces and at grain boundaries in oxides and carbides, Solid State Ionics. 12 (1984) 299–307. https://doi.org/10.1016/0167-2738(84)90159-0.

[22] A. Gil, O. Kryshtal, T. Brylewski, A. Czyrska-Filemonowicz, Characterization of a Cr2O3 scale formed on chromium with implanted yttrium ions by advanced electron microscopy, Surf. Coatings Technol. 368 (2019) 232–242. https://doi.org/10.1016/j.surfcoat.2019.03.081.

[23] H. Falk-Windisch, P. Malmberg, M. Sattari, J.-E. Svensson, J. Froitzheim, Determination of the oxide scale growth mechanism using 18O-tracer experiments in combination with Transmission Electron Microscopy and nanoscale Secondary Ion Mass Spectrometry, Mater. Charact. 136 (2018) 128–133. https://doi.org/10.1016/j.matchar.2017.12.001.

[24] C.M. Cotell, G.J. Yurek, R.J. Hussey, D.F. Mitchell, M.J. Graham, The influence of grain-boundary segregation of Y in Cr2O3 on the oxidation of Cr metal. II. Effects of temperature and dopant concentration, Oxid. Met. 34 (1990) 201–216. https://doi.org/10.1007/BF00665015.

[25] D. Clemens, V. Vosberg, W. Hobbs, U. Breuer, W.J. Quadakkers, H. Nickel, TEM and SNMS studies of protective alumina scales on NiCrAlY-alloys, Anal. Bioanal. Chem. 355 (1996) 703–706. https://doi.org/10.1007/s0021663550703.

[26] S.B. Newcomb, D.J. Smith, W.M. Stobbs, The application of high resolution electron microscopy to the study of oxidation, J. Microsc. 130 (1983) 137–146. https://doi.org/https://doi.org/10.1111/j.1365-2818.1983.tb04212.x.

[27] K. Przybylski, A.J. Garratt-Reed, G.J. Yurek, Grain Boundary Segregation of Yttrium in Chromia Scales, J. Electrochem. Soc. 135 (1988) 509–517. https://doi.org/10.1149/1.2095646.

[28] B. Gault, M.P. Moody, J.M. Cairney, S.P. Ringer, Atom Probe Microscopy, Springer New York, New York, NY, 2012. https://doi.org/10.1007/978-1-4614-3436-8.

[29] T.D. Nguyen, A. La Fontaine, L. Yang, J.M. Cairney, J. Zhang, D.J. Young, Atom probe

study of impurity segregation at grain boundaries in chromia scales grown in CO2 gas, Corros. Sci. 132 (2018) 125–135. https://doi.org/10.1016/j.corsci.2017.12.024.

[30] A. La Fontaine, H.-W. Yen, P.J. Felfer, S.P. Ringer, J.M. Cairney, Atom probe study of chromium oxide spinels formed during intergranular corrosion, Scr. Mater. 99 (2015) 1–4. https://doi.org/10.1016/j.scriptamat.2014.09.028.

[31] K. Stiller, L. Viskari, G. Sundell, F. Liu, M. Thuvander, H.-O. Andrén, D.J. Larson, T. Prosa, D. Reinhard, Atom Probe Tomography of Oxide Scales, Oxid. Met. 79 (2013) 227–238. https://doi.org/10.1007/s11085-012-9330-6.

[32] I. Povstugar, J. Weber, D. Naumenko, T. Huang, M. Klinkenberg, W.J. Quadakkers, Correlative Atom Probe Tomography and Transmission Electron Microscopy Analysis of Grain Boundaries in Thermally Grown Alumina Scale, Microsc. Microanal. 25 (2019) 11–20. https://doi.org/10.1017/S143192761801557X.

[33] J.-H. Kim, B.K. Kim, D.-I. Kim, P.-P. Choi, D. Raabe, K.-W. Yi, The role of grain boundaries in the initial oxidation behavior of austenitic stainless steel containing alloyed Cu at 700°C for advanced thermal power plant applications, Corros. Sci. 96 (2015) 52–66. https://doi.org/10.1016/j.corsci.2015.03.014.

[34] S. Pedrazzini, D.J. Child, G. West, S.S. Doak, M.C. Hardy, M.P. Moody, P.A.J. Bagot, Oxidation behaviour of a next generation polycrystalline Mn containing Ni-based superalloy, Scr. Mater. 113 (2016) 51–54. https://doi.org/10.1016/j.scriptamat.2015.10.001.

[35] Y. Chen, R.C. Reed, E.A. Marquis, Interfacial Solute Segregation in the Thermally Grown Oxide of Thermal Barrier Coating Structures, Oxid. Met. 82 (2014) 457–467. https://doi.org/10.1007/s11085-014-9502-7.

[36] T. Boll, K.A. Unocic, B.A. Pint, K. Stiller, Interfaces in Oxides Formed on NiAlCr Doped with Y, Hf, Ti, and B, Microsc. Microanal. 23 (2017) 396–403. https://doi.org/10.1017/S1431927617000186.

[37] G. Sundell, M. Thuvander, H.-O. Andrén, Enrichment of Fe and Ni at metal and oxide grain boundaries in corroded Zircaloy-2, Corros. Sci. 65 (2012) 10–12. https://doi.org/10.1016/j.corsci.2012.08.061.

[38] K.A. Unocic, Y. Chen, D. Shin, B.A. Pint, E.A. Marquis, STEM and APT characterization of scale formation on a La,Hf,Ti-doped NiCrAl model alloy, Micron. 109 (2018) 41–52.

https://doi.org/10.1016/j.micron.2018.01.011.

[39] P. Kontis, S. Pedrazzini, Y. Gong, P.A.J. Bagot, M.P. Moody, R.C. Reed, The effect of boron on oxide scale formation in a new polycrystalline superalloy, Scr. Mater. 127 (2017) 156–159. https://doi.org/10.1016/j.scriptamat.2016.09.013.

[40] W.J. Quadakkers, J. Piron-Abellan, V. Shemet, L. Singheiser, Metallic interconnectors for solid oxide fuel cells – a review, Mater. High Temp. 20 (2003) 115–127. https://doi.org/10.1179/mht.2003.015.

[41] K. Thompson, D. Lawrence, D.J. Larson, J.D. Olson, T.F. Kelly, B. Gorman, In situ site-specific specimen preparation for atom probe tomography, Ultramicroscopy. 107 (2007) 131–139. https://doi.org/10.1016/j.ultramic.2006.06.008.

[42] A. Vayyala, I. Povstugar, D. Naumenko, W.J. Quadakkers, H. Hattendorf, J. Mayer, A Nanoscale Study of Thermally Grown Chromia on High-Cr Ferritic Steels and Associated Oxidation Mechanisms, J. Electrochem. Soc. 167 (2020) 061502. https://doi.org/10.1149/1945-7111/ab7d2e.

[43] D. Monceau, B. Pieraggi, Determination of Parabolic Rate Constants from a Local Analysis of Mass-Gain Curves, Oxid. Met. 50 (1998) 477–493. https://doi.org/10.1023/A:1018860909826.

[44] W.J. Quadakkers, D. Naumenko, E. Wessel, V. Kochubey, L. Singheiser, Growth Rates of Alumina Scales on Fe–Cr–Al Alloys, Oxid. Met. 61 (2004) 17–37. https://doi.org/10.1023/B:OXID.0000016274.78642.ae.

[45] M. Karahka, H.J. Kreuzer, The Mystery of Missing Species in Atom Probe Tomography of Composite Materials, Microsc. Microanal. 22 (2016) 658–659. https://doi.org/10.1017/S1431927616004141.

[46] A. Devaraj, R. Colby, W.P. Hess, D.E. Perea, S. Thevuthasan, Role of Photoexcitation and Field Ionization in the Measurement of Accurate Oxide Stoichiometry by Laser-Assisted Atom Probe Tomography, J. Phys. Chem. Lett. 4 (2013) 993–998. https://doi.org/10.1021/jz400015h.

[47] N. Birks, G.H. Meier, F.S. Pettit, Introduction to the High Temperature Oxidation of Metals, Cambridge University Press, 2006. https://doi.org/10.1017/CBO9781139163903.

[48] W.J. Quadakkers, J. Żurek, Oxidation in Steam and Steam/Hydrogen Environments, in:

Shreir's Corros., Elsevier, 2010: pp. 407–456. https://doi.org/10.1016/B978-044452787-5.00022-6.

[49] M. Michalik, M. Hänsel, J. Zurek, L. Singheiser, W.J. Quadakkers, Effect of water vapour on growth and adherence of chromia scales formed on Cr in high and low pO 2 -environments at 1000 and 1050°C, Mater. High Temp. 22 (2005) 213–221. https://doi.org/10.1179/mht.2005.025.

[50] R.J.D. Tilley, Defects in Solids, John Wiley & Sons, Inc., Hoboken, NJ, USA, 2008. https://doi.org/10.1002/9780470380758.

[51] W.D. Kingery, Plausible Concepts Necessary and Sufficient for Interpretation of Ceramic Grain-Boundary Phenomena: I, Grain-Boundary Characteristics, Structure, and Electrostatic Potential, J. Am. Ceram. Soc. 57 (1974) 1–8. https://doi.org/10.1111/j.1151-2916.1974.tb11350.x.

[52] E. Essuman, G.H. Meier, J. Zurek, M. Hänsel, W.J. Quadakkers, The effect of water vapor on selective oxidation of Fe-Cr alloys, Oxid. Met. 69 (2008) 143–162. https://doi.org/10.1007/s11085-007-9090-x.

[53] D.J. Young, D. Naumenko, E. Wessel, L. Singheiser, W.J. Quadakkers, Effect of Zr Additions on the Oxidation Kinetics of FeCrAlY Alloys in Low and High pO2 Gases, Metall. Mater. Trans. A. 42 (2011) 1173–1183. https://doi.org/10.1007/s11661-010-0462-5.

[54] Z. Shen, D. Tweddle, H. Yu, G. He, A. Varambhia, P. Karamched, F. Hofmann, A.J. Wilkinson, M.P. Moody, L. Zhang, S. Lozano-Perez, Microstructural understanding of the oxidation of an austenitic stainless steel in high-temperature steam through advanced characterization, Acta Mater. 194 (2020) 321–336. https://doi.org/10.1016/j.actamat.2020.05.010.

[55] A. Rahmel, J. Tobolski, Einfluss von wasserdampf und kohlendioxyd auf die oxydation von eisen in sauerstoff bei hohen temperaturen, Corros. Sci. 5 (1965) 333–346. https://doi.org/10.1016/S0010-938X(65)90500-7.

[56] C.T. Fujii, R.A. Meussner, The Mechanism of the High-Temperature Oxidation of Iron-Chromium Alloys in Water Vapor, J. Electrochem. Soc. 111 (1964) 1215. https://doi.org/10.1149/1.2425963.

[57] J. Quadakkers, L. Singheiser, Practical Aspects of the Reactive Element Effect, Mater.

Sci. Forum. 369–372 (2001) 77–92.

https://doi.org/10.4028/www.scientific.net/MSF.369-372.77.